




Article

# Simple Approach to the Fabrication of Lanthanum Orthoniobates and Nanocomposites with Ni, Cu, and Co Metal Nanoparticles Using Supercritical Isopropanol

Dinara Altynbekova <sup>1</sup>, Yuliya Bepalko <sup>2,\*</sup> , Konstantin Valeev <sup>2</sup>, Nikita Ereemeev <sup>2</sup>, Ekaterina Sadovskaya <sup>2</sup>, Tamara Krieger <sup>2</sup>, Artem Ulihin <sup>3</sup>, Arina Uhina <sup>3</sup>, Bakytgul Massalimova <sup>1</sup>, Mikhail Simonov <sup>2</sup>  and Vladislav Sadykov <sup>2</sup> 

- <sup>1</sup> Chemistry and Chemical Technology Department, Taraz Regional University Named after M. Kh. Dulaty, Suleimanova 6, 080000 Taraz, Kazakhstan
- <sup>2</sup> Heterogeneous Catalysis Department, Federal Research Center Boreskov Institute of Catalysis SB RAS, Akad. Laverntieva Ave. 5, 630090 Novosibirsk, Russia
- <sup>3</sup> Laboratory of Solid State Ionic, Institute of Solid State Chemistry and Mechanochemistry SB RAS, Kutateladze Str. 18, 630128 Novosibirsk, Russia
- \* Correspondence: bepalko@catalysis.ru



**Citation:** Altynbekova, D.; Bepalko, Y.; Valeev, K.; Ereemeev, N.; Sadovskaya, E.; Krieger, T.; Ulihin, A.; Uhina, A.; Massalimova, B.; Simonov, M.; et al. Simple Approach to the Fabrication of Lanthanum Orthoniobates and Nanocomposites with Ni, Cu, and Co Metal Nanoparticles Using Supercritical Isopropanol. *J. Compos. Sci.* **2022**, *6*, 243. <https://doi.org/10.3390/jcs6090243>

Academic Editor: Konda Gokuldoss Prashanth

Received: 31 July 2022

Accepted: 18 August 2022

Published: 23 August 2022

**Publisher's Note:** MDPI stays neutral with regard to jurisdictional claims in published maps and institutional affiliations.



**Copyright:** © 2022 by the authors. Licensee MDPI, Basel, Switzerland. This article is an open access article distributed under the terms and conditions of the Creative Commons Attribution (CC BY) license (<https://creativecommons.org/licenses/by/4.0/>).

**Abstract:** Orthoniobates of rare-earth elements are a promising group of materials attractive for the design of nanocomposite hydrogen separation membranes owing to a perspective type of proton conductivity, good mechanical properties, and high stability in H<sub>2</sub>O- and CO<sub>2</sub>-containing atmospheres. In general, the promising method involves the synthesis of nanocomposites with transition metals (Cu, Ni, and Cu-Ni alloys) and their oxides with high electronic conductivity. For the first time, lanthanum orthoniobates and nanocomposites with NiCu and NiCo nanoparticles were synthesized using alcohol solutions of salts of the corresponding metals by the solvothermal method in a flow reactor in a supercritical isopropanol medium. This method made it possible to obtain single-phase La<sub>0.99</sub>Ca<sub>0.01</sub>NbO<sub>4-δ</sub> oxide. The introduction of doping titanium cations did not allow obtaining a single-phase La<sub>0.99</sub>Ca<sub>0.01</sub>Nb<sub>0.98</sub>Ti<sub>0.02</sub>O<sub>4-δ</sub> sample, as impurities in lanthanum methaniobate and La<sub>2</sub>Ti<sub>2</sub>O<sub>7</sub> were found. Calcined powders and gastight pellets of orthoniobates and nanocomposites were characterized by X-ray diffraction analysis as well as scanning and transmission electron microscopy. Transport characteristics were investigated by the Van der Pauw technique, varying measurement temperatures in a wet H<sub>2</sub> atmosphere. The oxygen mobility was estimated by the oxygen isotope heteroexchange with C<sup>18</sup>O<sub>2</sub>.

**Keywords:** orthoniobate; nanocomposite; supercritical fluids; membrane; conductivity

## 1. Introduction

The finding and development of suitable materials for the creation of energy conversion and storage devices based on inorganic ceramic elements continue to this day. An active search for materials considered promising ionic conductors thanks to high values of proton and oxygen conductivity, density, and thermochemical stability is underway [1–3]. These include orthoniobates of rare-earth elements, which are characterized as perspective materials for use as components of fuel cells and other electrochemical devices such as membranes for oxygen and hydrogen separation, ceramic membrane reactors, and electrolyzers [4–9].

Lanthanum orthoniobates have been considered as promising proton-conducting solid electrolytes over the past decade. These materials have good chemical stability in atmospheres containing CO<sub>2</sub> and H<sub>2</sub>O, unlike barium cerates and zirconates [10]. However, despite the high stability, these compounds have a rather low conductivity compared with the materials mentioned above [11].

The value of proton conductivity depends on the defect structure of the oxide, as the presence of oxygen vacancies is the main factor responsible for the appearance of proton defects. Thus, the introduction of additional cations into the perovskite structure with a natural deficiency of the oxygen sublattice leads to a further increase in structural disorder and, as a result, to an increase in proton conductivity. Many efforts have been made to improve the conductivity by single- or multi-element doping. A further increase in the mobility of protons in materials based on  $\text{LaNbO}_4$  was achieved by doping its A-sublattice with cations of a lower valence and a larger ionic radius, such as Sr, Ce, Yb, Pr, Mg, Cu, and Ca [12–20], as well as doping its B-sublattice with cations having a high valence with a small ionic radius, such as W, Al, Zr, Ti, Co, Mo, and Ta [21–28]. Despite the acceptor nature of Ti-doping, there is an indication of n-type conductivity at 1000 °C for the Ti-doped sample. One may thus suggest that the multivalent nature of Ti slightly reduces the effective band gap and, consequently, increases the concentration of electrons. This behaviour is in agreement with the interpretation of the dependence of the bulk conductivity as a function of  $\text{pH}_2\text{O}$  at 1200 °C [28].

To create highly efficient proton-conducting membranes, materials of the functional layer should be used with a set of characteristics, such as stability in various media ( $\text{CO}_2$ ,  $\text{H}_2\text{O}$ ), high mechanical strength, and high conductivity. It is not always possible for individual components to meet these requirements, so approaches such as the use of composites will help to solve this problem. In particular, lanthanum orthoniobates with high stability in a humid and carbon-dioxide-containing atmosphere, good mechanical properties, compatibility with transition metals (Cu, Ni, and Cu–Ni alloys) and their oxides, and sufficiently high ionic conductivity make these compounds attractive for the development of nanocomposite materials for hydrogen separation membranes [4,29,30]. The introduction of another component such as a metal into the composite provides mechanical strength high electronic conductivity, which is crucial to avoid hydrogen permeation limiting by coupled electron–proton transport across the membrane.

There are various methods for the synthesis of proton-conducting lanthanum orthoniobate, such as the most commonly used solid-phase method [16,19,23,24,27–30], the method of mechanical activation [13,31], the molten salt method [32], the sol–gel method [33], and spray pyrolysis from aqueous precursors [14,34]. Most of the methods listed above are multi-stage, require a long processing time, and entail significant energy consumption.

A relatively recently proposed method for the synthesis of nanomaterials in supercritical fluids, thanks to their unique properties (low viscosity, lack of surface tension, high supersaturation of the solution, and so on), provides a high-performance synthesis of materials with the required properties. Moreover, because of the high rate of particle formation in supercritical fluids, this method allows synthesis in a continuous stream. Here, the synthesis process can be modified by changing the operating parameters, so elucidation of how each parameter affects the process allows to control the structure, particles' size, and morphology of materials [35]. Alkali niobates nanoparticles were continuously synthesized in a supercritical water flow system [36]. Single-phase  $\text{NaNbO}_3$  was obtained under supercritical conditions over a wide range of parameters ( $T > 400$  °C,  $25 < p < 30$  MPa). Besides, metal nanopowders and nanocomposites were synthesized in supercritical fluids [37].

In the work of [38], a possibility to carry out reduction reactions of metal oxides and salts in supercritical isopropanol media was shown. A number of oxides (CuO, CdO, HgO,  $\text{Co}_x\text{O}_y$ ,  $\text{Bi}_2\text{O}_3$ , and so on) can be used for the synthesis of functional materials based on metal particles fixed on various supports. Nanoparticles of Ni, Cu, and Ag metals were synthesized continuously in supercritical methanol with the formation of very small particles, and this method provided an alternative pre-annealing treatment that improves the sinterability of materials and decreases the temperature of sintering [39]. In previous studies [40], we obtained metals and alloys based on nickel, copper, cobalt, and silver. The results of our research showed that using supercritical alcohols allows for obtaining metals and alloys in one stage. The powders after calcination are spherical nanoparticles with an average size of 25–45 nm.

In this study, we report that NiCu and NiCo nanoparticles and orthoniobates powders can be synthesized using supercritical alcohol fluid technology. Moreover, for the first time, new types of nanocomposites containing metal ( $M = \text{Ni, Co, Cu}$ ) nanoparticles and niobates were prepared. The properties (size, phase composition, and morphology) of the synthesized materials were characterized by scanning electron microscopy (SEM), transmission electron microscopy (HRTEM), and X-ray diffraction analysis. Transport properties (conductivity and oxygen mobility) of obtained materials were investigated. While single-phase rare-earth niobates have already been studied well, based on them, nanocomposite materials with mixed conductivity of both theoretical and practical interest were prepared and characterized for the first time.

## 2. Materials and Methods

Samples of oxides and nanocomposites were synthesized by solvothermal synthesis using supercritical alcohols in a flow-through reactor. The experimental custom-built setup for the preparation of materials is described elsewhere [41].

Materials were synthesized using alcohol solutions of salts of corresponding metals  $\text{La}(\text{NO}_3)_3 \cdot 6\text{H}_2\text{O}$  (99.99% Vecton, Saint-Petersburg, Russia),  $\text{Ca}(\text{NO}_3)_2$  (99.5% Reakhim, Moscow, Russia)  $\text{NbCl}_5$  (99.99% Acros Organics, Geel, Belgium),  $\text{Co}(\text{NO}_3)_2 \cdot 6\text{H}_2\text{O}$  (99.90% Reakhim, Moscow, Russia),  $\text{Ni}(\text{NO}_3)_2 \cdot n\text{H}_2\text{O}$  (Reakhim, Moscow, Russia),  $\text{Cu}(\text{NO}_3)_2 \cdot 6\text{H}_2\text{O}$  (99.5% Vecton, Saint-Petersburg, Russia), and  $\text{C}_{16}\text{H}_{36}\text{O}_4\text{Ti}$  (99.99% Alfa Aesar, Karlsruhe, Germany). Precursor solutions were prepared by dissolving salts in isopropanol (99.99% Reakhim, Moscow, Russia) with the addition of an equimolar amount of acetylacetonate (99.99% Reakhim, Moscow, Russia) as a complexing agent. Ni/Co and Ni/Cu molar ratios were equal to 1. A mixture of metal solutions was fed into a U-shaped reactor ( $l = 75$  cm, inner diameter = 4 mm) at a rate of 5 mL/min. At the same time, isopropyl alcohol preheated to a temperature of 150 °C was fed into the reactor at a rate of 9 mL/min at 400 °C and a pressure of 120 atm. The synthesis products were separated from the mother liquor by decantation. The precipitates were dried and calcined under air for 4 h (NiCu and NiCo at 500 °C and orthoniobates at 1100 °C).

For «one-pot» synthesis of nanocomposites  $\text{La}_{0.99}\text{Ca}_{0.01}\text{NbO}_4/\text{NiCuO}_x$  and  $\text{La}_{0.99}\text{Ca}_{0.01}\text{NbO}_4/\text{NiCoO}_x$  (65:35 wt.%) in supercritical conditions, the required quantities of corresponding salts were blended in isopropanol with the addition of acetylacetonate as a complexing agent. The mixed solution was fed into a reactor and SCS was performed under the same conditions as for niobates. All precursors were dried at 80 °C for 12 h and calcined under air at 1100 °C for 6 h.

All powders of nanocomposites were pressed into pellets of 10–12 mm in diameter and sintered by the hot-pressing technique under 50 MPa at 1100 °C for 15 min in Ar. The pellets of orthoniobates powders were sintered at 1100 °C for 4 h in air.

The codes and compositions of samples of Ni-Co, Ni-Cu, and orthoniobates, as well as nanocomposites based on them, are presented in Table 1.

**Table 1.** Properties of materials.

№	Code	Composition	Relative Density, %	SSA, m <sup>2</sup> /g	
				700 °C	1100 °C
1	LCNb	$\text{La}_{0.99}\text{Ca}_{0.01}\text{NbO}_4$	77	13	1.5
2	LCNbTi	$\text{La}_{0.99}\text{Ca}_{0.01}\text{Nb}_{0.98}\text{Ti}_{0.02}\text{O}_{4-\delta}$	74	14.6	5.9
3	NiCu	$\text{Ni}_{0.5}\text{Cu}_{0.5}\text{O}_x$	-	8 *	-
4	NiCo	$\text{Ni}_{0.5}\text{Co}_{0.5}\text{O}_x$	-	10 *	-
5	NiCu-LCNb	$\text{La}_{0.99}\text{Ca}_{0.01}\text{NbO}_4/\text{NiCuO}_x$	82	4.5	0.3
6	NiCo-LCNb	$\text{La}_{0.99}\text{Ca}_{0.01}\text{NbO}_4/\text{NiCoO}_x$	85	5.3	0.1

\* Experiments were carried out for samples calcined at 500 °C.

All calcined powders and gas-tight pellets of orthoniobates and nanocomposites were characterized by X-ray diffraction, transmission electron microscopy (TEM), scanning electron microscopy (SEM), specific surface area, conductivity, and oxygen mobility measurements. Diffraction patterns were obtained using a Bruker diffractometer Advance D8 with  $\text{CuK}\alpha$  radiation. Scanning was carried out in the range of angles of 15–90 ( $2\theta$ ) with a scanning step of 0.05 ( $2\theta$ ). The identification of the obtained phases and quantitative calculations were obtained using the ICDD X-ray data file.

Measurements of the textural characteristics of materials were carried out by physical adsorption of  $\text{N}_2$  using an ASAP-2400 (Micromeritics Instrument. Corp., Norcross, GA, USA). The specific surface area (SSA) was calculated using obtained adsorption isotherms.

$\text{La}_{0.99}\text{Ca}_{0.01}\text{Nb}_{0.98}\text{Ti}_{0.02}\text{O}_{4-\delta}$  sample was examined using an FIB-SEM microscope (Tesla Solaris, Brno-Kohoutovice, Czech Republic) equipped with secondary and reflected electron detectors. Samples in the form of pellets were attached to a standard holder followed by spraying a thin carbon layer to ensure the conductivity of the near-surface layer. The other samples were investigated using high-angle ring scanning electron microscopy in a dark field (HAADF-STEM). High-resolution transmission electron microscopy (HRTEM) data were obtained using a JEM-2200FS transmission electron microscope (JEOL Ltd., Tokyo, Japan, accelerating voltage 200 kV, grating resolution of 1Å) equipped with a Cs corrector and an EDX spectrometer (JEOL Ltd., Tokyo, Japan). The minimum spot diameter for step-by-step line analysis or mapping of elementary EDX analysis was  $\sim 1$  nm, with a step of about 1.5 nm. Fourier-Raman spectra ( $3600\text{--}100\text{ cm}^{-1}$ , 300 scans, resolution  $4\text{ cm}^{-1}$ , geometry  $180^\circ$ ) were recorded using a Bruker RFS 100/S spectrometer.

Electrical conductivity was studied by impedance spectroscopy in two electrode cells placed in a humid hydrogen atmosphere using a precision LCR HP-4284AP meter in the AC frequency range of  $20\text{ Hz}^{-1}$  MHz. Bulk conductivity values were determined from analysis of the  $Z''\text{--}Z'$  plots. The proton conductivity of composites containing metal alloys was determined on compact samples by the four-probe van der Pauw method in the galvanostatic mode with four ion-selective probes made of proton-conducting  $\text{La}_{0.99}\text{Ca}_{0.01}\text{NbO}_4$  ceramics, similar to the ion probe technique described elsewhere [42]. Ion-selective electrodes allow the determination of proton conductivity, as they completely block the electron current, while being reversible electrodes for protons.

The theoretical density and porosity of the pelletized composites were investigated by Archimedes' method.

The oxygen mobility and surface reactivity of the milled samples were studied using temperature-programmed isotope exchange of oxygen (TPIE) with  $\text{C}^{18}\text{O}_2$  in the flow reactor. Samples were loaded into the quartz tube with an inner diameter of 3 mm. Pretreatment was carried out in  $\text{He} + 1\% \text{O}_2$  feed with a flow rate of 25 mL/min at  $700^\circ\text{C}$  for 0.5 h. TPIE experiments were carried out in  $\text{He} + 1\% \text{C}^{18}\text{O}_2$  gas mixture with a flow rate of 25 mL/min while heating from  $50^\circ\text{C}$  to  $700\text{--}800^\circ\text{C}$  with a ramp of  $5^\circ\text{C}/\text{min}$ . The outlet gas mixture was analyzed by an UGA 200 mass spectrometer (Stanford Research Systems, Stanford Research Systems Inc., Sunnyvale, CA, USA). The temperature dependencies of  $^{18}\text{O}$  atoms ( $\alpha$ ) and  $\text{C}^{16}\text{O}^{18}\text{O}$  molecules ( $f_{16-18}$ ) mole fractions were analyzed to calculate the oxygen tracer diffusion coefficient ( $D^*$ ) and its effective activation energy ( $E_a, D$ ) values using a mathematical model [43].

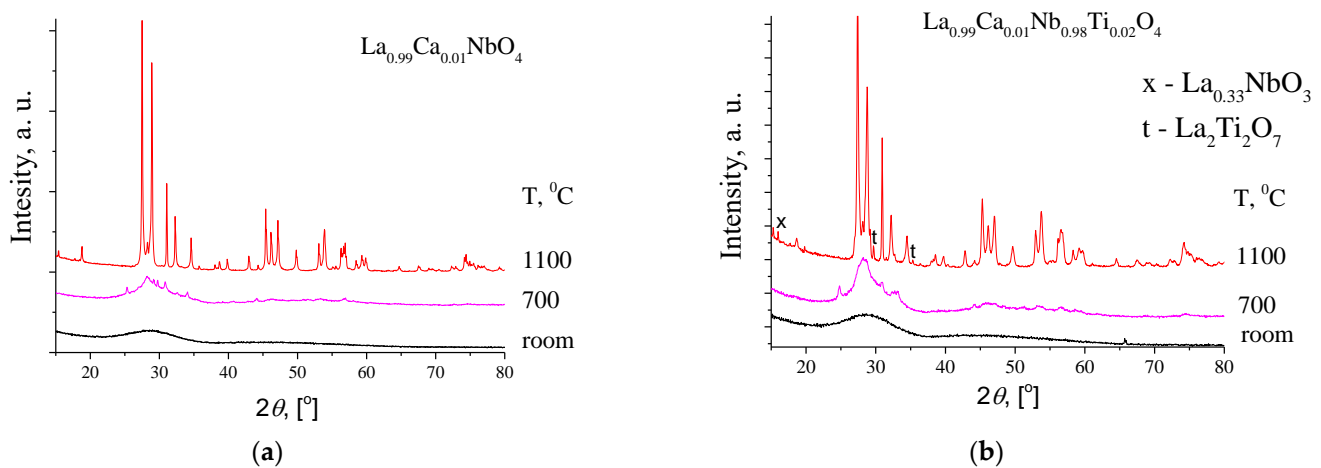
### 3. Results and Discussion

#### 3.1. Structural Characteristics

##### 3.1.1. Niobates

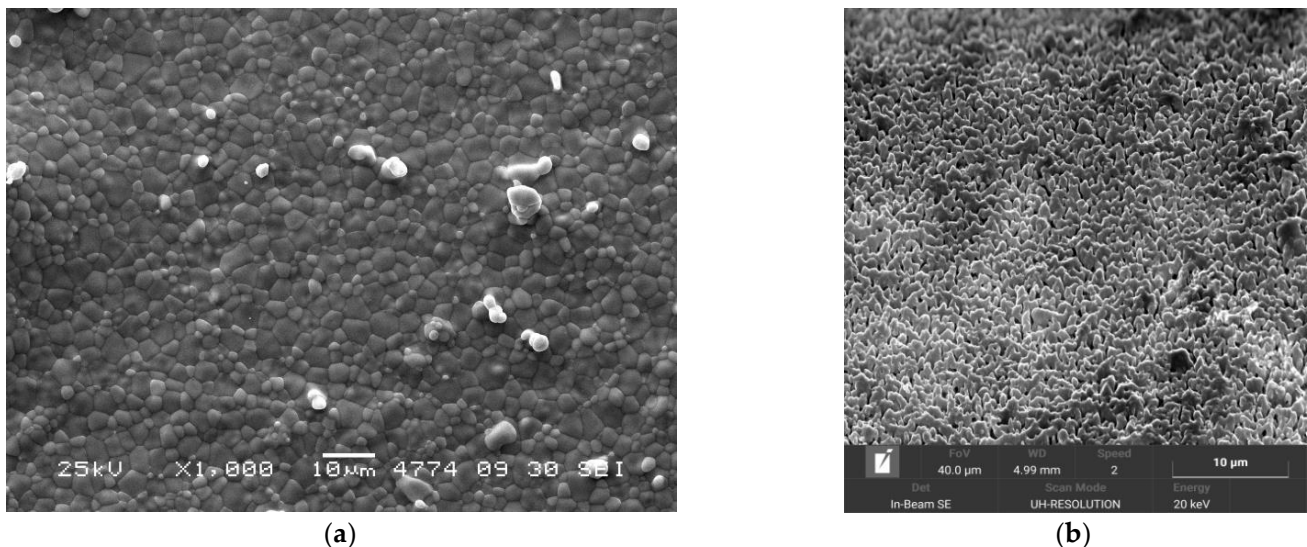
According to the diffraction patterns in Figure 1, both lanthanum orthoniobates after supercritical synthesis are X-ray amorphous materials. The formation of the orthoniobate phase only began after calcination at  $700^\circ\text{C}$ . Figure 1a demonstrates XRD patterns of the  $\text{La}_{0.99}\text{Ca}_{0.01}\text{NbO}_4$  (LCNb) sample, and only reflections of the fergusonite phase with monoclinic structure (PDF [01-083-1911]) are observed for samples calcined at  $1100^\circ\text{C}$ .





**Figure 1.** XRD patterns of (a) LCNb and (b) LCNbTi sintered at different temperatures.

In contrast, the powder of  $\text{La}_{0.99}\text{Ca}_{0.01}\text{Nb}_{0.98}\text{Ti}_{0.02}\text{O}_{4-\delta}$  (LCNbTi) calcined at  $1100\text{ }^{\circ}\text{C}$  is a mixture of three phases—monoclinic  $\text{LaNbO}_{4-\delta}$  (PDF [01-083-1911]) and low quantities of monoclinic  $\text{La}_2\text{Ti}_2\text{O}_7$  (PDF [00-028-0517]) and orthorhombic  $\text{La}_{0.33}\text{NbO}_3$  (PDF [00-026-0822]) phases (Figure 2b). The impurity  $\text{La}_{0.33}\text{NbO}_3$  is a mixed electronic and ionic (oxygen-ion and proton) conductor depending on temperature and conditions [44]. The presence of this impurity can also lead to an increase in the proton conductivity.



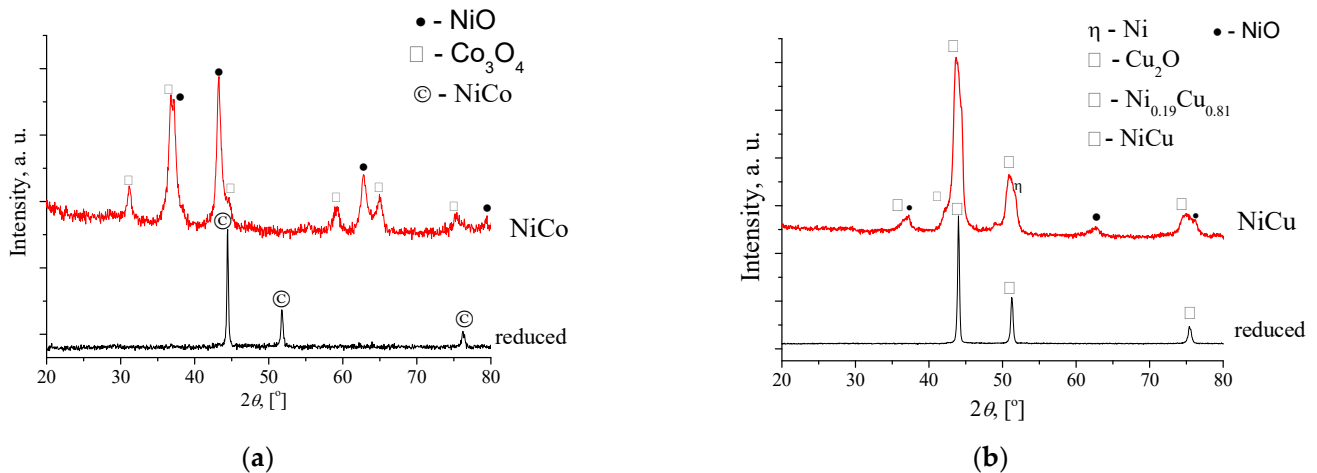
**Figure 2.** SEM images of (a) LCNb and (b) LCNbTi after calcination at  $1100\text{ }^{\circ}\text{C}$ .

Figure 2 shows the SEM images of LCNb and LCNbTi powders sintered at  $1100\text{ }^{\circ}\text{C}$  for 4 h. The  $\text{La}_{0.99}\text{Ca}_{0.01}\text{NbO}_4$  sample is quite dense and pore-free, with similar grain sizes in the range of  $2\text{--}6\text{ }\mu\text{m}$  (Figure 2a). Titanium-doped lanthanum orthoniobate is still very porous after 4 h of sintering, with a grain size distribution varying from  $1\text{ to }4\text{ }\mu\text{m}$  (Figure 2b).

### 3.1.2. NiCu and NiCo

According to the XRD data, weakly crystallized phases of solid solutions of nickel, copper, and cobalt oxides are present immediately after drying the obtained suspension. During synthesis in supercritical medium, nickel–copper alloys were obtained, and the metal cations were reduced in the reactor as a result of the interaction with supercritical isopropanol. Based on XRD data (Figure 3a) after treatment at  $500\text{ }^{\circ}\text{C}$  in the air, the NiCo

sample is a mixture of nickel and cobalt oxide. The unit cell parameter of  $\text{Co}_3\text{O}_4$  is 8.101 Å and that of NiO is 4.174 Å. The average crystallite size is 22.5 and 16.0 nm, respectively. As follows from the XRD patterns for the reduced NiCo sample (Figure 2a), the lattice constant is 3.534 Å. For metallic cobalt and nickel, the cell parameter is 3.544 Å (PDF [89-4307]) and 3.524 Å (PDF [65-2865]), respectively. Based on this, according to Vegard's rule, the unit cell parameter corresponds to an Ni/Co ratio of ~50/50.



**Figure 3.** XRD patterns of the (a) NiCo and (b) NiCu powdered samples calcined at 500 °C in air (curves NiCu and NiCo) and after treatment at 600 °C in hydrogen (reduced).

The NiCu powdered sample calcined at 500 °C is a mixture of  $\text{Ni}_{0.19}\text{Cu}_{0.81}$  alloy, nickel, NiO, and  $\text{Cu}_2\text{O}$  phases (Figure 3b). For metallic Cu, the lattice parameter is 3.625 Å (PDF [70-3038]) and that of Ni is 3.524 Å (PDF [65-2865]). After reduction of this sample, the lattice parameter of the metal phase was changed to 3.563 Å, which corresponded to Ni/Cu alloy with a composition ~60/40.

The TEM data of NiCo and NiCu samples show almost spherical metal nanoparticles with an average size of 10–45 nm (Figure 4).

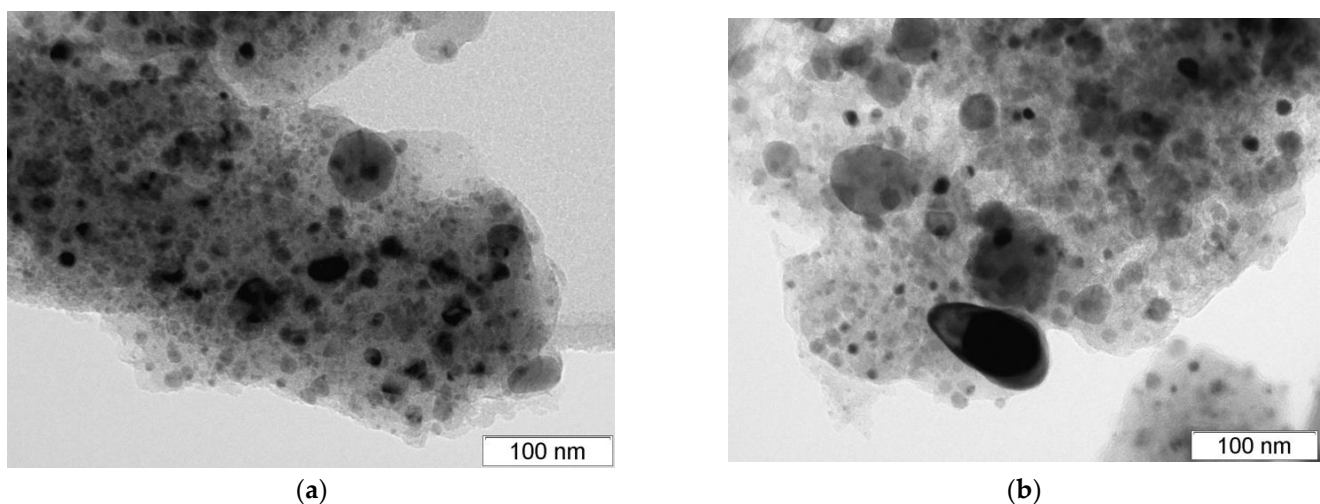


**Figure 4.** TEM images of (a) NiCo and (b) NiCu after calcination at 500 °C.

### 3.1.3. Nanocomposites

Modification in the phase composition of nanocomposites with the increase in calcination temperature is shown in Figure 5. During the synthesis of nanocomposites, there was no reduction in nickel, copper, or cobalt to the metallic state. For materials after calcination

at 500 °C under air, the phases of nickel and cobalt oxides were formed, while the phase of lanthanum orthoniobate had not yet crystallized. For NiCo–LCNb nanocomposite sintered at 700 °C, the main phase is monoclinic  $\text{La}_{0.99}\text{Ca}_{0.01}\text{NbO}_4$ , with NiO and  $\text{Co}_3\text{O}_4$  phases being observed as well. With a further increase in calcination temperature under air up to 1100 °C, a phase of mixed nickel–cobalt oxide was formed.

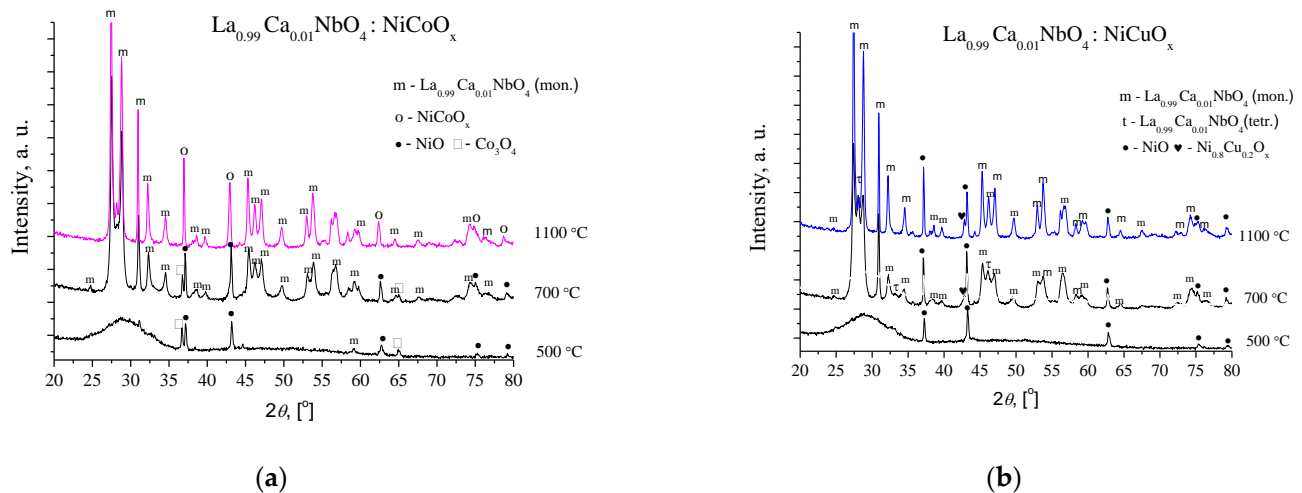


**Figure 5.** XRD patterns of the composites NiCo–LCNb (a) and NiCu–LCNb (b) sintered at 500–1100 °C.

The nanocomposite NiCu–LCNb (700 °C) consists of monoclinic and tetragonal phases of the composition  $\text{La}_{0.99}\text{Ca}_{0.01}\text{NbO}_4$ , nickel oxide NiO, and a solid solution of nickel–copper oxide  $\text{Ni}_{0.8}\text{Cu}_{0.2}\text{O}_x$  (Figure 5b). Reflections corresponding to a separate copper phase or its oxides were not observed; hence, copper compounds are apparently in X-ray amorphous states. There were no new phases indicating products of chemical interaction between components of nanocomposites.

According to scanning transmission electron microscopy (HAADF-STEM), both samples showed a rather uniform spatial cation distribution (Figures 6 and 7). In the NiCu–LCNb sample, the distribution of lanthanum, niobium, and copper is uniform, but relatively large nickel particles are observed. The ratio of nickel to copper depends on the survey area, thus, unlike copper, nickel is unevenly distributed, which agrees with the assumption that copper is predominantly in fine form or distributed in the volume of lanthanum–calcium niobate. As for the NiCo–LCNb sample, the distribution of all elements is more uniform (Figure 7).

### 3.2. Reducibility in Hydrogen

Temperature-programmed reduction (TPR) was performed for lanthanum orthoniobate and for nanocomposites sintered at different temperatures (Figure 8). La orthoniobate is almost not reducible by hydrogen in the analyzed temperature range. The lower temperature TPR peaks at 214–240 °C and 400–436 °C correspond to the reduction of NiO to Ni, CuO to Cu,  $\text{Co}_3\text{O}_4$  to CoO, and CoO to Co [45]. As shown in our previous work [46], the recovery of a nickel–copper alloy in its pure form takes place at 201 °C, and in composites containing NiCu and tungstates, the peak shifted towards higher temperatures of 254–312 °C. This was explained by the partial decoration of NiCuO particles in nanocomposites with tungstates oxide fragments, which reduces their reactivity. A similar situation is observed in the case of NiCu–LCNb and NiCo–LCNb nanocomposites.

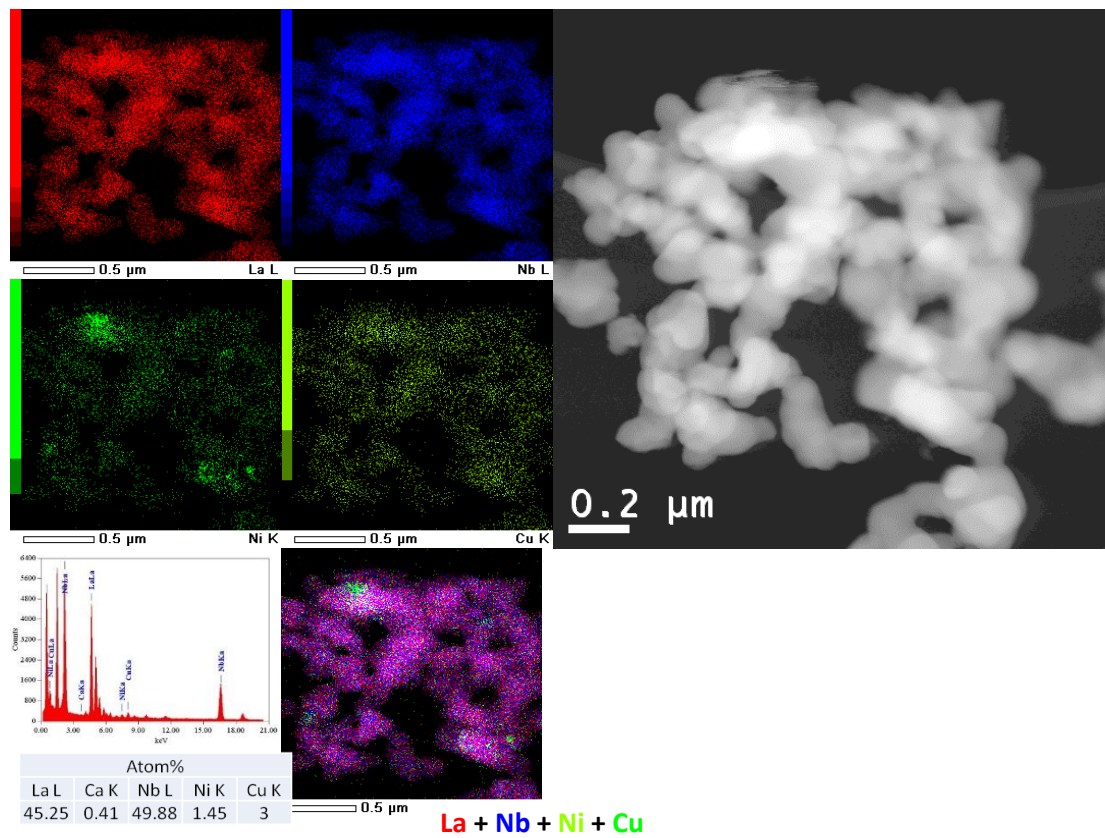


Figure 6. HAADF-STEM image with EDX analysis of  $\text{La}_{0.99}\text{Ca}_{0.01}\text{NbO}_4/\text{NiCuO}_x$ .

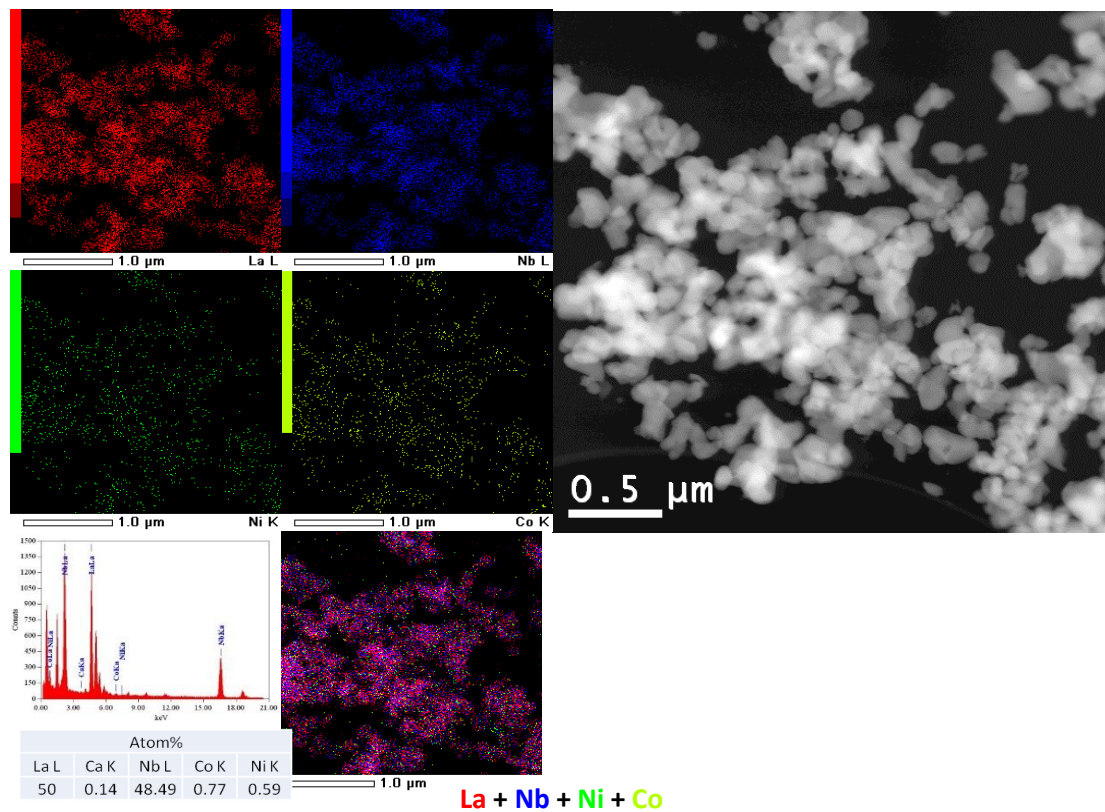
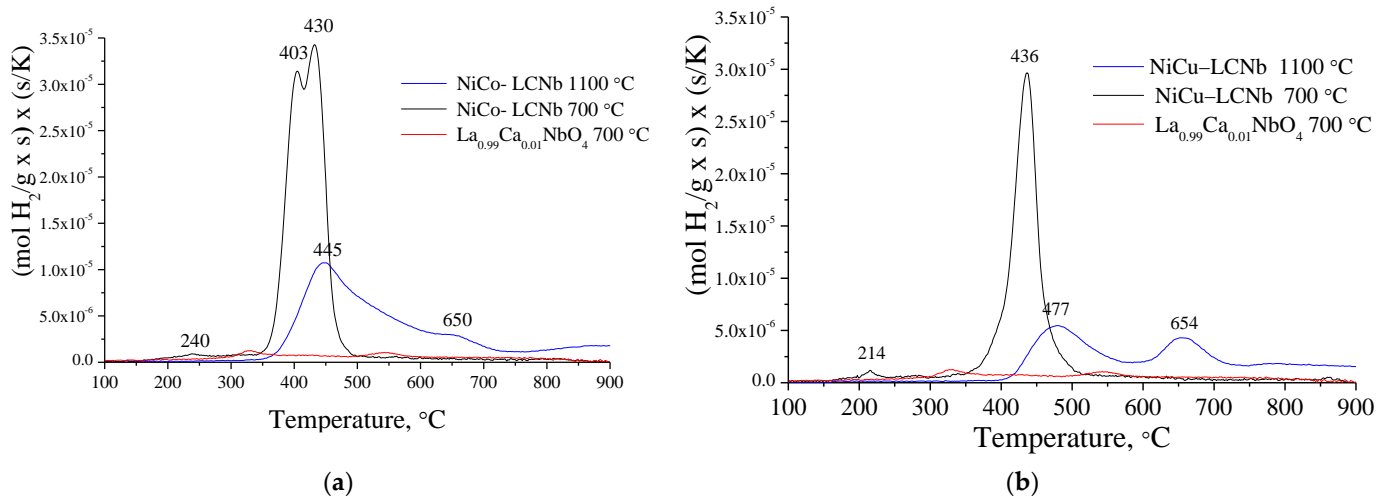


Figure 7. HAADF-STEM image with EDX analysis of  $\text{La}_{0.99}\text{Ca}_{0.01}\text{NbO}_4/\text{NiCoO}_x$ .





**Figure 8.** TPR-H<sub>2</sub> spectra of lanthanum orthoniobate LCNb and composites: (a) NiCo-LCNb and (b) NiCu-LCNb composites as powders sintered at 700 and 1100 °C.

For both composites calcined at 1100 °C, reduction peaks are shifted to higher temperatures as compared with samples after calcination at 700 °C, while the amounts of removed oxygen decreases. Figure 9 shows the diffraction patterns of composites where, in addition to the main phase of lanthanum orthoniobate, phases of NiCo and NiCu alloys are obtained. Hydrogen consumption during NiCo-LCNb composite reduction is larger than that for NiCu-LCNb, as displayed in Table 2.

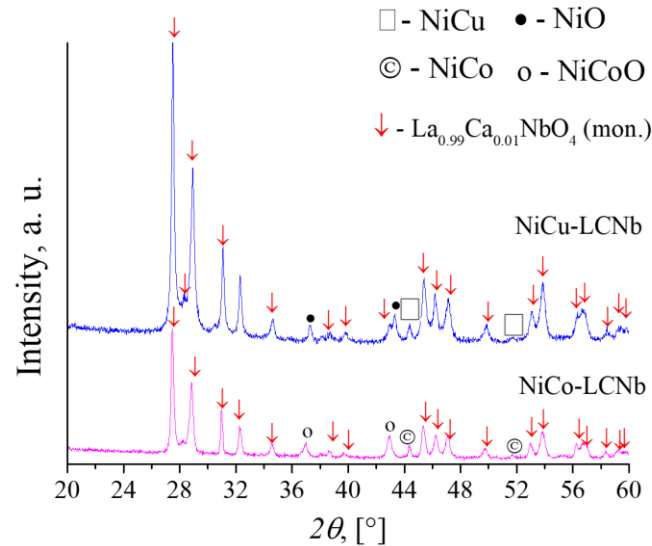


**Figure 9.** XRD patterns of the composites after reducing treatment at 600 °C for 2 h in H<sub>2</sub>/Ar.

**Table 2.** Characteristics of H<sub>2</sub>-TPR spectra.

№	Sample	T <sub>calcination</sub> , °C	The Maxima of Peaks, °C		H <sub>2</sub> Consumption, mol H <sub>2</sub> g <sup>-1</sup> × 10 <sup>-3</sup>
			T <sub>1</sub>	T <sub>2</sub>	
1	LCNb	700	325	544	0.4
2	NiCu-LCNb	700	436	-	1.8
		1100	477	654	1.3
3	NiCo-LCNb	700	403	430	2.8
		1100	445	-	2.1

### 3.3. Conductivity

The electric conductivity of composites was studied for their pellets calcined at 1100 °C. According to XRD data (Figure 9), after reduction in H<sub>2</sub>, the monoclinic phase of lanthanum orthoniobate was present in both nanocomposites. Ni and Ni-Co oxides partially disappeared with formation of Ni-Co alloy. The NiCu alloy phase was detected in the XRD patterns of the NiCu-LCNb composite. Figure 10 shows SEM micrographs of composites after calcination at 1100 °C. This method of nanocomposites' preparation provides a high density of nanocomposite ceramics (Table 1).

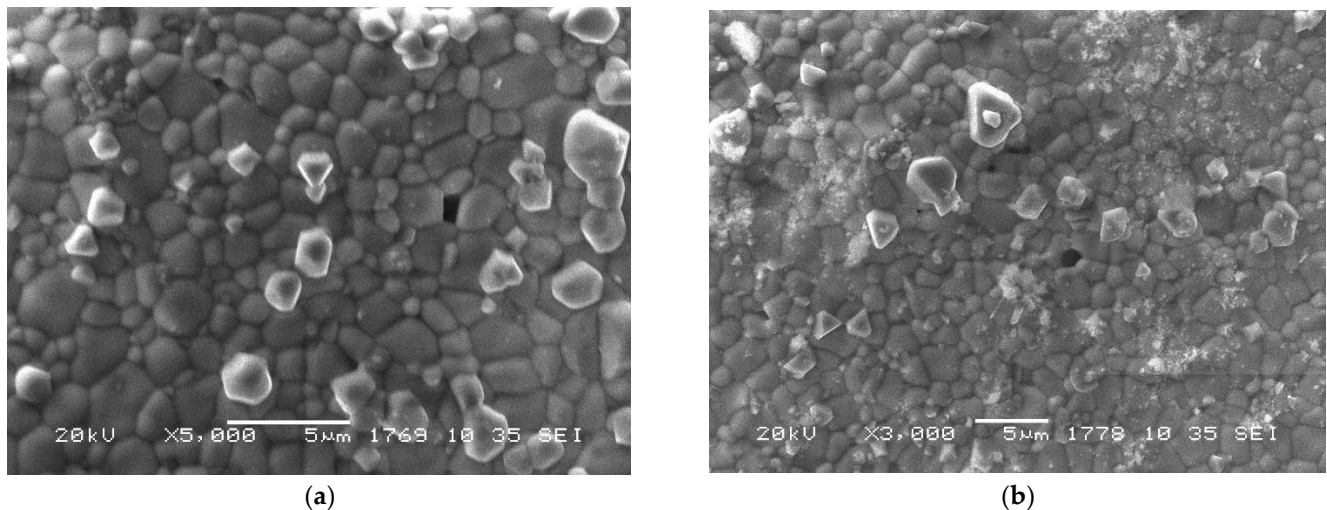
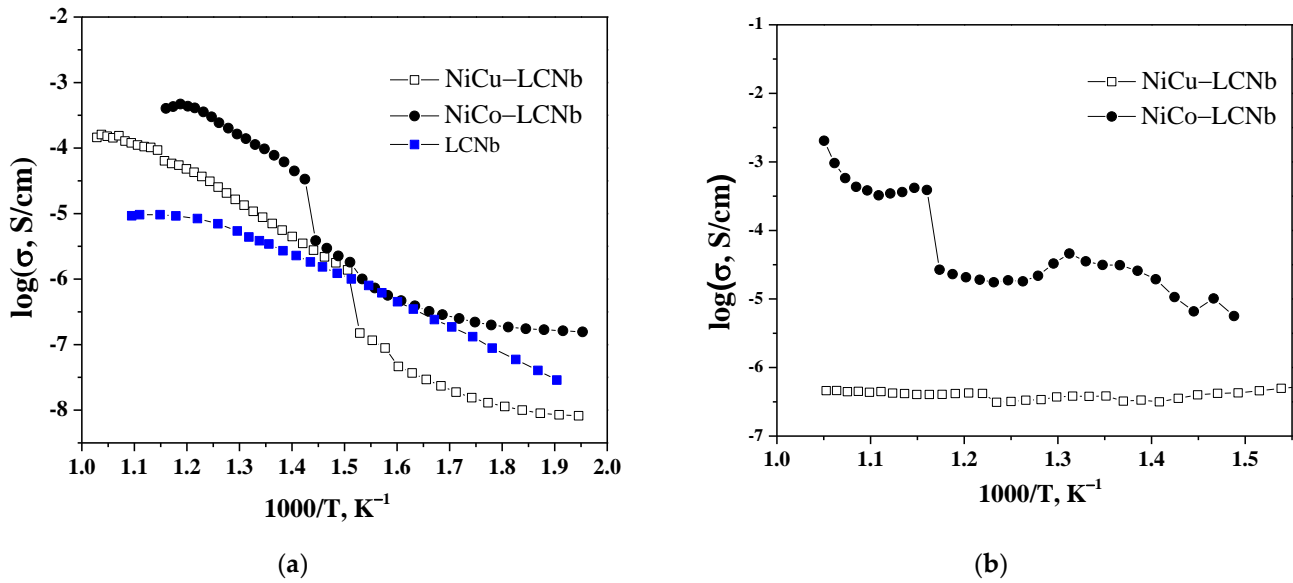


**Figure 10.** SEM images of the composites (a) NiCu-LCNb and (b) NiCo-LCNb after calcination at 1100 °C.

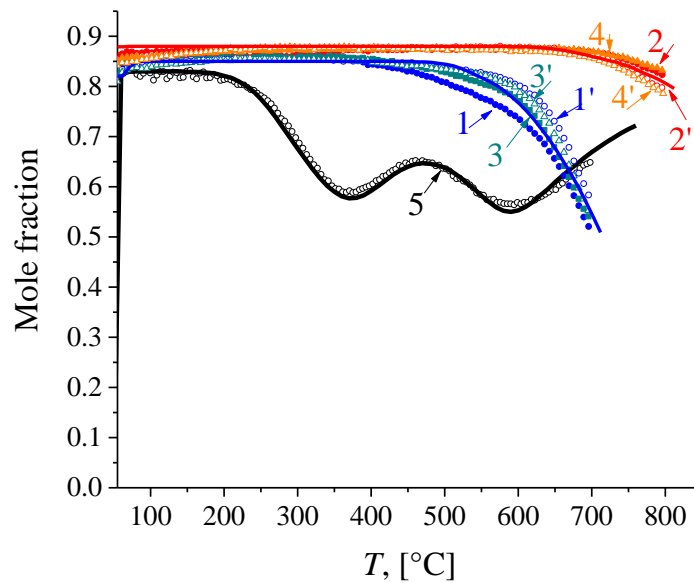
Temperature dependences of the conductivity of nanocomposites are presented in Figure 11. To prevent oxidation of metals, the measurements were carried out in an atmosphere of moist hydrogen. Their total electrical conductivity is high, up to  $10^{-3}$  S/cm. Lanthanum orthoniobate doped with Ca exhibits the highest proton conductivity of the orthoniobates, up to  $\sim 1 \times 10^{-4}$  S/cm in wet reducing conditions at 700 °C [15,23,44]. Figure 11a shows that nanocomposite materials have high electronic and ionic conductivity. Figure 11b shows the experimental temperature dependences of proton conductivity of NiCu-LCNb and NiCo-LCNb obtained using a four-electrode cell with ion probe electrodes. The NiCo-LCNb nanocomposite shows high values of both electronic and proton conductivity.

### 3.4. Oxygen Mobility

Figure 12 demonstrates the TPIE curves of NiCu-LCNb and NiCo-LCNb composites. For comparison reasons, the TPIE curve for the LCNb sample obtained in the previous work [4] is added as well. The diffusion rate for composites catastrophically declines compared with that of LCNb. One can suppose that such a drastic decrease in oxygen mobility is associated with a negative effect of nickel-copper/cobalt oxides having very low oxide ionic conductivity [4,43,47]. It is likely that such an effect includes partial blocking of oxide-ionic conductive LCNb particles by relatively large nickel-copper/cobalt oxide particles. Reduction of these particles can partially unlock the LCNb phase, as the metallic particles are small (Section 3.1).



**Figure 11.** Total electric conductivity (a) and proton conductivity (b) of pelletized nanocomposites in wet He + 10% H<sub>2</sub> gas mixture.

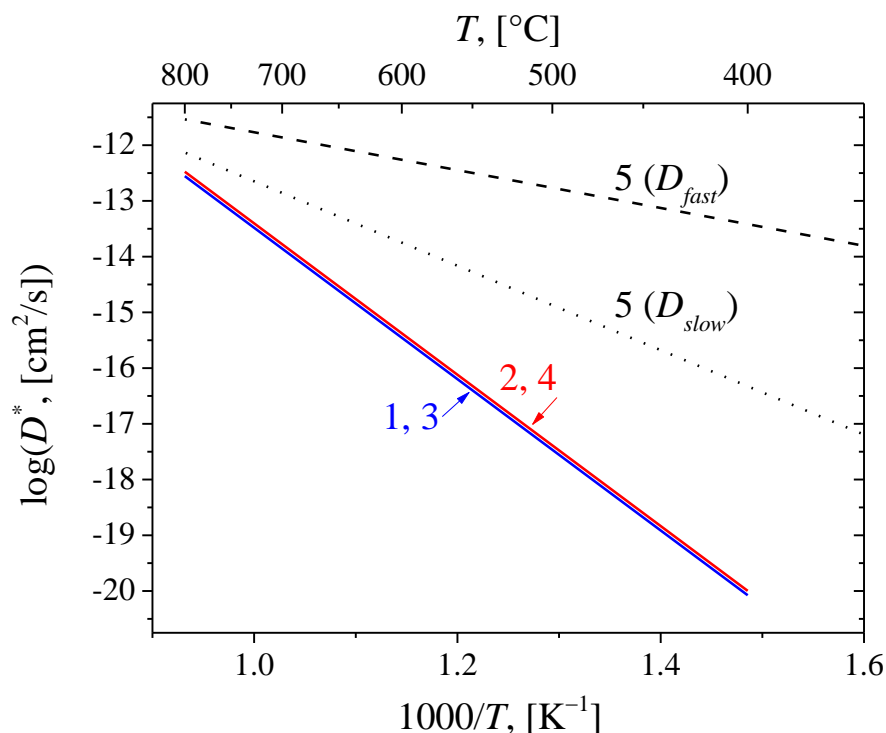


**Figure 12.** Temperature-programmed isotope of oxygen with C<sup>18</sup>O<sub>2</sub> in an open reactor for samples: 1,1'—NiCu-LCNb sintered at 700 °C, 2,2'—NiCu-LCNb sintered at 1100 °C, 3,3'—NiCo-LCNb sintered at 700 °C, 4,4'—NiCo-LCNb sintered at 1100 °C, and 5—LCNb [4]; 1–4 —initial samples, 1'–4'—samples after reduction and reoxidation. Points—experiment, lines—modelling.

However, reduction of the samples by hydrogen (in He + H<sub>2</sub> flow at 600 °C for 1 h) followed by soft reoxidation (in He + CO<sub>2</sub> flow at 800 °C for 1 h) did not demonstrate a significant increase in oxygen diffusivity (Figure 12, curves 1'–4'). The effective activation energy (E<sub>a,D</sub>) value was 260 kJ/mol (Table 3, Figure 13). The oxygen tracer diffusion coefficient (D\*) values were close for all samples (~10<sup>-20</sup> cm<sup>2</sup>/s at 700 K), with visible differences in the isotope substitution rate being generally related to the difference in the SSA, and hence in the diffusion path.

**Table 3.** The oxygen tracer diffusion coefficient values at 700 K and its effective activation energy for NiCu–LCNb and NiCo–LCNb samples according to TPIE with  $C^{18}O_2$  data modelling.

Sample	$T_{\text{calcination}}, ^\circ\text{C}$	$D^*  _{700\text{ K}}, [\text{cm}^2/\text{s}]$	$E_{a,D}, [\text{kJ/mol}]$
NiCu–LCNb	700	$5(\pm 3) \cdot 10^{-20}$	260
	1100	$6(\pm 4) \cdot 10^{-20}$	
NiCo–LCNb	700	$5(\pm 3) \cdot 10^{-20}$	
	1100	$6(\pm 4) \cdot 10^{-20}$	

**Figure 13.** Arrhenius plots of tracer diffusion coefficient for NiCu–LCNb (1, 2) and NiCo–LCNb (3, 4) samples sintered at 700 °C (1,3) and 1100 °C (2,4) compared with LCNb sample (5) [4], according to TPIE with  $C^{18}O_2$  data modelling.

#### 4. Conclusions

In the present work, proton solid electrolytes  $La_{0.99}Ca_{0.01}NbO_4$  and  $La_{0.99}Ca_{0.01}Nb_{0.98}Ti_{0.02}O_{4-\delta}$ , metal alloys NiCo and NiCu, and metal–ceramic nanocomposites  $La_{0.99}Ca_{0.01}NbO_4/NiCuO_x$  and  $La_{0.99}Ca_{0.01}NbO_4/NiCoO_x$  were prepared using supercritical media, and their structural and transport properties were characterized. For the first time, an approach of one-pot synthesis of nanocomposites was developed using continuous solvothermal flow synthesis in supercritical isopropanol. This route is a promising technique for the synthesis of single-phase initial electrolytes, alloys, and nanocomposites. High-density ceramics by sintering of powders at 1100 °C using the hot pressure technique were developed. Composites based on La orthoniobates with a high conductivity are promising materials for hydrogen separation membranes.

**Author Contributions:** Conceptualization, Y.B. and V.S.; investigation, K.V., A.U. (Artem Ulihin), A.U. (Arina Uhina), N.E., E.S. and T.K.; writing—original draft preparation, D.A. and Y.B.; writing—review and editing, Y.B. and V.S.; supervision, V.S. and B.M.; project administration, M.S. All authors have read and agreed to the published version of the manuscript.

**Funding:** This work was funded by the Ministry of Science and Higher Education of the Russian Federation within the governmental order for Boreskov Institute of Catalysis (project AAAA-A21-121011390054-1).



**Institutional Review Board Statement:** Not applicable.

**Informed Consent Statement:** Informed consent was obtained from all subjects involved in the study.

**Data Availability Statement:** Not applicable.

**Acknowledgments:** The research was performed using equipment of Shared Knowledge Center “National Center of Catalyst Research” (Boreskov Institute of Catalysis SB RAS), Novosibirsk, Russia as well as Taraz Regional University named after M. Kh. Dulaty, Taraz, Kazakhstan.

**Conflicts of Interest:** The authors declare no conflict of interest.

## References

1. Kim, J.; Sengodan, S.; Kim, S.; Kwon, O.; Bu, Y.; Kim, G. Proton conducting oxides: A review of materials and applications for renewable energy conversion and storage. *Renew. Sustain. Energy Rev.* **2019**, *109*, 606–618. [[CrossRef](#)]
2. Lei, L.; Zhang, J.; Yuan, Z.; Liu, J.; Ni, M.; Chen, F. Progress Report on Proton Conducting Solid Oxide Electrolysis Cells. *Adv. Funct. Mater.* **2019**, *29*, 1903805. [[CrossRef](#)]
3. Haider, R.; Wen, Y.; Ma, Z.-F.; Wilkinson, D.P.; Zhang, L.; Yuan, X.; Song, S.; Zhang, J. High temperature proton exchange membrane fuel cells: Progress in advanced materials and key technologies. *Chem. Soc. Rev.* **2020**, *50*, 1138–1187. [[CrossRef](#)] [[PubMed](#)]
4. Sadykov, V.A.; Bepalko, Y.N.; Krasnov, A.V.; Skriabin, P.I.; Lukashevich, A.I.; Fedorova, Y.E.; Sadovskaya, E.M.; Ereemeev, N.F.; Krieger, T.A.; Ishchenko, A.V.; et al. Novel proton-conducting nanocomposites for hydrogen separation membranes. *Solid State Ion.* **2018**, *322*, 69–78. [[CrossRef](#)]
5. Solís, C.; Serra, J.M. Adjusting the conduction properties of  $\text{La}_{0.995}\text{Ca}_{0.005}\text{NbO}_{4-\delta}$  by doping for proton conducting fuel cells electrode operation. *Solid State Ion.* **2011**, *190*, 38–45. [[CrossRef](#)]
6. Nico, C.; Monteiro, T.; Graça, M.P.F. Niobium oxides and niobates physical properties: Review and prospects. *Prog. Mater. Sci.* **2016**, *80*, 1–37. [[CrossRef](#)]
7. Harris, C.M.; Skinner, S.J. Redox behaviour and solid solubility of cerium ortho-niobates. *J. Solid State Chem.* **2019**, *271*, 135–143. [[CrossRef](#)]
8. Magrasó, A.; Haugsrud, R.; Norby, T. Preparation and characterization of Ni-LaNbO<sub>4</sub> cermet anode supports for proton-conducting fuel cell applications. *J. Am. Ceram. Soc.* **2010**, *93*, 2650–2655. [[CrossRef](#)]
9. Chiara, A.; Canu, G.; Longo, A.; Pipitone, C.; Martorana, A.; Giannici, F. Solid-state compatibility of Ca:LaNbO<sub>4</sub> with perovskite cathodes: Evidences from X-ray microspectroscopy. *Electrochim. Acta* **2022**, *401*, 139495. [[CrossRef](#)]
10. Medvedev, D.A.; Lyagaeva, J.G.; Gorbova, E.V.; Demin, A.K.; Tsiakaras, P. Advanced materials for SOFC application: Strategies for the development of highly conductive and stable solid oxide proton electrolytes. *Prog. Mater. Sci.* **2016**, *75*, 38–79. [[CrossRef](#)]
11. Norby, T.; Haugsrud, R. *Dense Ceramic Membranes for Hydrogen Separation*; Wiley-VCH Verlag GmbH & Co. KGaA: Weinheim, Germany, 2006; ISBN 3527313427.
12. Mokkelbost, T.; Lein, H.L.; Vullum, P.E.; Holmestad, R.; Grande, T.; Einarsrud, M.A. Thermal and mechanical properties of LaNbO<sub>4</sub>-based ceramics. *Ceram. Int.* **2009**, *35*, 2877–2883. [[CrossRef](#)]
13. Cao, Y.; Duan, N.; Yan, D.; Chi, B.; Pu, J.; Jian, L. Enhanced electrical conductivity of LaNbO<sub>4</sub> by A-site substitution. *Int. J. Hydrog. Energy* **2016**, *41*, 20633–20639. [[CrossRef](#)]
14. Syvertsen, G.E.; Magrasó, A.; Haugsrud, R.; Einarsrud, M.A.; Grande, T. The effect of cation non-stoichiometry in LaNbO<sub>4</sub> materials. *Int. J. Hydrog. Energy* **2012**, *37*, 8017–8026. [[CrossRef](#)]
15. Ivanova, M.; Ricote, S.; Meulenberg, W.A.; Haugsrud, R.; Ziegner, M. Effects of A- and B-site (co-)acceptor doping on the structure and proton conductivity of LaNbO<sub>4</sub>. *Solid State Ion.* **2012**, *213*, 45–52. [[CrossRef](#)]
16. Dzierzgowski, K.; Wachowski, S.; Gojtowska, W.; Lewandowska, I.; Jasiński, P.; Gazda, M.; Mielewczyk-Gryń, A. Praseodymium substituted lanthanum orthoniobate: Electrical and structural properties. *Ceram. Int.* **2018**, *44*, 8210–8215. [[CrossRef](#)]
17. Fjeld, H.; Kepaptsoglou, D.M.; Haugsrud, R.; Norby, T. Charge carriers in grain boundaries of 0.5% Sr-doped LaNbO<sub>4</sub>. *Solid State Ion.* **2010**, *181*, 104–109. [[CrossRef](#)]
18. Cao, Y.; Chi, B.; Pu, J.; Jian, L. Effect of Ce and Yb co-doping on conductivity of LaNbO<sub>4</sub>. *J. Eur. Ceram. Soc.* **2014**, *34*, 1981–1988. [[CrossRef](#)]
19. Hakimova, L.; Kasyanova, A.; Farlenkov, A.; Lyagaeva, J.; Medvedev, D.; Demin, A.; Tsiakaras, P. Effect of isovalent substitution of La<sup>3+</sup> in Ca-doped LaNbO<sub>4</sub> on the thermal and electrical properties. *Ceram. Int.* **2019**, *45*, 209–215. [[CrossRef](#)]
20. Dzierzgowski, K.; Wachowski, S.; Łapiński, M.; Mielewczyk-Gryń, A.; Gazda, M. Praseodymium Orthoniobate and Praseodymium Substituted Lanthanum Orthoniobate: Electrical and Structural Properties. *Materials* **2022**, *15*, 2267. [[CrossRef](#)]
21. Canu, G.; Giannici, F.; Chiara, A.; Confalonieri, G.; Longo, A.; Teresa, M.; Dapiaggi, M.; Buscaglia, V.; Martorana, A. combined synchrotron techniques: Structure, W oxidation state and interdiffusion. *J. Alloys Compd.* **2021**, *857*, 157532. [[CrossRef](#)]
22. Li, M.; Wu, R.; Zhu, L.; Cheng, J.; Hong, T.; Xu, C. Enhanced sinterability and conductivity of cobalt doped lanthanum niobate as electrolyte for proton-conducting solid oxide fuel cell. *Ceram. Int.* **2019**, *45*, 573–578. [[CrossRef](#)]
23. Brandão, A.D.; Gracio, J.; Mather, G.C.; Kharton, V.V.; Fagg, D.P. B-site substitutions in  $\text{LaNb}_{1-x}\text{MxO}_{4-\delta}$  materials in the search for potential proton conductors (M=Ga, Ge, Si, B, Ti, Zr, P, Al). *J. Solid State Chem.* **2011**, *184*, 863–870. [[CrossRef](#)]

24. Cao, Y.; Duan, N.; Wang, X.; Chi, B.; Pu, J.; Jian, L. Enhanced electrical conductivity of Mo-doped LaNbO<sub>4</sub>. *J. Eur. Ceram. Soc.* **2015**, *35*, 1979–1983. [[CrossRef](#)]
25. Sayers, R.; Kilner, J.A.; Skinner, S.J. *Investigation of Ruddlesden-Popper Based Materials for Cathode Applications in Intermediate Temperature Sofcs*; Imperial College London: London, UK, 2008; Volume 135, p. 2725.
26. Li, C.; Bayliss, R.D.; Skinner, S.J. Crystal structure and potential interstitial oxide ion conductivity of LnNbO<sub>4</sub> and LnNb<sub>0.92</sub>W<sub>0.08</sub>O<sub>4.04</sub> (Ln = La, Pr, Nd). *Solid State Ion.* **2014**, *262*, 530–535. [[CrossRef](#)]
27. Bi, Z.; Bridges, C.A.; Kim, J.H.; Huq, A.; Paranthaman, M.P. Phase stability and electrical conductivity of Ca-doped LaNb<sub>1-x</sub>Ta<sub>x</sub>O<sub>4-δ</sub> high temperature proton conductors. *J. Power Sources* **2011**, *196*, 7395–7403. [[CrossRef](#)]
28. Huse, M.; Norby, T.; Haugrud, R. Effects of A and B site acceptor doping on hydration and proton mobility of LaNbO<sub>4</sub>. *Int. J. Hydrog. Energy* **2012**, *37*, 8004–8016. [[CrossRef](#)]
29. Magrasó, A.; Fontaine, M.L. Investigation of compatible anode systems for LaNbO<sub>4</sub>-based electrolyte in novel proton conducting solid oxide fuel cells. *J. Power Sources* **2011**, *196*, 10183–10190. [[CrossRef](#)]
30. Lee, H.W.; Park, J.H.; Nahm, S.; Kim, D.W.; Park, J.G. Low-temperature sintering of temperature-stable LaNbO<sub>4</sub> microwave dielectric ceramics. *Mater. Res. Bull.* **2010**, *45*, 21–24. [[CrossRef](#)]
31. Maschio, S.; Bachiarrini, A.; Di Monte, R.; Montanaro, L. Preparation and characterization of LaNbO<sub>4</sub> from amorphous precursors. *J. Mater. Sci.* **1995**, *30*, 5433–5437. [[CrossRef](#)]
32. Mielewczyk-Gryn, A.; Wachowski, S.; Zagórski, K.; Jasiński, P.; Gazda, M. Characterization of magnesium doped lanthanum orthoniobate synthesized by molten salt route. *Ceram. Int.* **2015**, *41*, 7847–7852. [[CrossRef](#)]
33. Bruncková, H.; Medvecký, L.; Hvizdoš, P.; Ďurišin, J.; Girman, V. Structural and mechanical properties of sol-gel prepared pyrochlore lanthanum niobates. *J. Mater. Sci.* **2015**, *50*, 7197–7207. [[CrossRef](#)]
34. Mokkelbost, T.; Kaus, I.; Haugrud, R.; Norby, T.; Grande, T.; Einarsrud, M.A. High-temperature proton-conducting lanthanum ortho-niobate-based materials. Part II: Sintering properties and solubility of alkaline earth oxides. *J. Am. Ceram. Soc.* **2008**, *91*, 879–886. [[CrossRef](#)]
35. Aymonier, C.; Loppinet-Serani, A.; Reverón, H.; Garrabos, Y.; Cansell, F. Review of supercritical fluids in inorganic materials science. *J. Supercrit. Fluids* **2006**, *38*, 242–251. [[CrossRef](#)]
36. Toyama, S.; Hayashi, H.; Takesue, M.; Watanabe, M.; Smith, R.L. Synthesis of alkali niobate K<sub>1-x</sub>Na<sub>x</sub>NbO<sub>3</sub> nanoparticles using a supercritical water flow system. *J. Supercrit. Fluids* **2016**, *107*, 1–8. [[CrossRef](#)]
37. Reverchon, E.; Adami, R. Nanomaterials and supercritical fluids. *J. Supercrit. Fluids* **2006**, *37*, 1–22. [[CrossRef](#)]
38. Ivicheva, S.N.; Kargin, Y.F.; Gorelik, V.S. Opal-matrix nanocomposites containing metallic nanoparticles. *Inorg. Mater.* **2015**, *51*, 840–847. [[CrossRef](#)]
39. Choi, H.; Veriansyah, B.; Kim, J.; Kim, J.D.; Kang, J.W. Continuous synthesis of metal nanoparticles in supercritical methanol. *J. Supercrit. Fluids* **2010**, *52*, 285–291. [[CrossRef](#)]
40. Altynbekova, D.; Massalimova, B.; Bepalko, Y.; Valeev, K.; Sadykov, V. *Synthesis of Metal Nanoparticles and Their Alloys Using Supercritical Fluids*; Her. Kazakh-British Technical University: Almaty, Kazakhstan, 2020; p. 17.
41. Bepalko, Y.; Smal, E.; Simonov, M.; Valeev, K.; Fedorova, V. Novel Ni/Ce(Ti) ZrO<sub>2</sub> catalysts for methane dry reforming prepared in supercritical alcohol media. *Energies* **2020**, *13*, 3365. [[CrossRef](#)]
42. Uvarov, N.F.; Ulihin, A.S.; Bepalko, Y.N.; Ereemeev, N.F.; Krasnov, A.V.; Skriabin, P.I.; Sadykov, V.A. Study of proton conductivity of composite metal-ceramic materials based on neodimium tugsates using a four-electrode technique with ionic probes. *Int. J. Hydrog. Energy* **2018**, *43*, 19521–19527. [[CrossRef](#)]
43. Sadykov, V.A.; Sadovskaya, E.M.; Ereemeev, N.F.; Skriabin, P.I.; Krasnov, A.V.; Bepalko, Y.N.; Pavlova, S.N.; Fedorova, Y.E.; Pikalova, E.Y.; Shlyakhtina, A.V. Oxygen Mobility in the Materials for Solid Oxide Fuel Cells and Catalytic Membranes (Review). *Russ. J. Electrochem.* **2019**, *55*, 701–718. [[CrossRef](#)]
44. Xing, W.; Syvertsen, G.E.; Grande, T.; Li, Z.; Haugrud, R. Hydrogen permeation, transport properties and microstructure of Ca-doped LaNbO<sub>4</sub> and LaNb<sub>3</sub>O<sub>9</sub> composites. *J. Membr. Sci.* **2012**, *415*, 878–885. [[CrossRef](#)]
45. Luisetto, I.; Tuti, S.; Di Bartolomeo, E. Co and Ni supported on CeO<sub>2</sub> as selective bimetallic catalyst for dry reforming of methane. *Int. J. Hydrog. Energy* **2012**, *37*, 15992–15999. [[CrossRef](#)]
46. Bepalko, Y.; Sadykov, V.; Ereemeev, N.; Skryabin, P.; Krieger, T.; Sadovskaya, E.; Bobrova, L.; Uvarov, N.; Lukashevich, A.; Krasnov, A.; et al. Synthesis of tungstates/Ni<sub>0.5</sub>Cu<sub>0.5</sub>O nanocomposite materials for hydrogen separation cermet membranes. *Compos. Struct.* **2018**, *202*, 1263–1274. [[CrossRef](#)]
47. Haugrud, R.; Norby, T. High-temperature proton conductivity in acceptor-doped LaNbO<sub>4</sub>. *Solid State Ion.* **2006**, *177*, 1129–1135. [[CrossRef](#)]